



AIAA 2000-0256

**A Computational Model for Rotor-Fuselage
Interactional Aerodynamics**

D. Douglas Boyd, Jr. and Richard W. Barnwell
Virginia Polytechnic Institute and State University
Virginia Consortium of Engineering and Sciences Universities
Hampton, Virginia

Susan Althoff Gorton
Aeroflightdynamics Directorate (AvRDEC)
U.S. Army Aviation and Missile Command
NASA Langley Research Center
Hampton, Virginia

**38th Aerospace Sciences
Meeting & Exhibit**

January 10-13, 2000/Reno, NV

A COMPUTATIONAL MODEL FOR ROTOR-FUSELAGE INTERACTIONAL AERODYNAMICS

D. Douglas Boyd, Jr.* and Richard W. Barnwell†
Virginia Polytechnic Institute and State University
Virginia Consortium of Engineering and Sciences Universities
Hampton, Virginia

Susan Althoff Gorton‡
Aeroflightdynamics Directorate (AvRDEC)
U.S. Army Aviation and Missile Command
NASA Langley Research Center
Hampton, Virginia

Abstract

A novel unsteady rotor-fuselage interactional aerodynamics model has been developed. This model loosely couples a Generalized Dynamic Wake Theory (GDWT) to a thin-layer Navier-Stokes solution procedure. This coupling is achieved using an unsteady pressure jump boundary condition in the Navier-Stokes model. The new unsteady pressure jump boundary condition models each rotor blade as a moving pressure jump which travels around the rotor azimuth and is applied between two adjacent planes in a cylindrical, non-rotating grid. Comparisons are made between measured and predicted time-averaged and time-accurate rotor inflow ratios. Additional comparisons are made between measured and predicted unsteady surface pressures on the top centerline and sides of the fuselage.

Introduction

It is well known that rotorcraft aerodynamics is a complicated topic. Due to the combination of various systems associated with rotorcraft, these aerodynamic phenomena are unsteady, even in level, unaccelerated flight. Complicating these issues are the facts that typical rotorcraft in service today have bluff aft regions, which can lead to large regions of flow separation, and that there can be significant aerodynamic interaction or interference between the rotating and non-rotating components of the system.

When designing a new rotorcraft, as with any flight vehicle, an understanding of the aerodynamic environment, including aerodynamic interaction of the different vehicle components, is essential. These interactional effects have been known and categorized for many years. This paper focuses on the “rotor-fuselage” and “fuselage-rotor” subsets of the categories offered by Sheridan and Smith.¹ In practice, information on specific interactional effects may be obtained using any combination of wind tunnel testing and/or computational modeling.

Wind tunnel testing has been relied upon heavily in designing new rotorcraft and diagnosing and correcting aerodynamic anomalies discovered on actual flight vehicles because computational modeling of rotorcraft aerodynamics is still in its infancy and lags well behind the computational capabilities used for fixed wing vehicle modeling. Several factors have led to this situation. One of these is the fact that, as mentioned above, even in level, unaccelerated flight, a rotorcraft is operating in an unsteady aerodynamic environment due to the rotation of the rotor system. A fixed wing aircraft in the same situation would be in a steady state environment. The computational implication of this is that a complete rotorcraft simulation would necessarily be a time-accurate computation, whereas the fixed wing simulation could be a steady-state computation. Another factor is associated with the vastly different time and length scales associated with rotorcraft. Some unsteady aerodynamic events, such as blade-vortex interaction, occur at length scales that are a small fraction of a blade chord and at time scales that are equivalent to a tiny fraction of a rotor revolution. To capture these effects, very small time steps would be required. However, determining the trim state of a rotorcraft requires balancing the gross forces on the rotorcraft that have a length scale on the order of the ro-

*Senior Research Associate, AIAA Member

†Professor, AIAA Fellow

‡Aerospace Engineer

Copyright ©2000 by the American Institute of Aeronautics and Astronautics, Inc. No copyright is asserted in the United States under Title 17, U.S. Code. The U.S. Government has a royalty-free license to exercise all rights under the copyright claimed herein for government purposes. All other rights are reserved by the copyright owner.

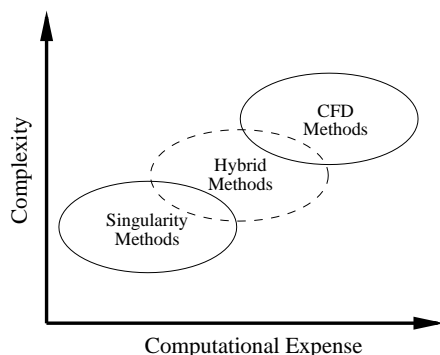


Figure 1. Analysis types for coupled solutions.

tor radius (*i.e.*, many chord lengths) over a relatively long time scale, equivalent to a number of rotor revolutions. The computational implication of these vastly different time scales is that a time-accurate simulation would need to be executed for many time steps.

There are a number of methods available for computation of the interactional aerodynamic effects associated with rotorcraft. Figure 1 categorizes these methods into three areas: Singularity Methods, Hybrid Methods, and Computational Fluid Dynamic (CFD) Methods. Each of these methods has been used in the past for computation of rotorcraft interactional aerodynamics, and each method has advantages and disadvantages.

Singularity Methods

Singularity methods typically use linear superpositions of solutions of Laplace's equation (*i.e.*, source, sink, doublet, vortex elements) to model systems that may include the fuselage, the fuselage wake, the rotor blades, and the rotor wake. Johnson² provides an extensive discussion of singularity methods used for rotorcraft analyses up through the year 1986. Boyd³ discusses other examples of analyses along these lines that have been published since that time. These analyses have shown varying degrees of success. It is apparent from these references that (1) one of the primary advantages of these methods is that they are typically computationally efficient and (2) one of the primary disadvantages is the inability to adequately account for viscous effects.

CFD Methods

In recent years, CFD methods, including methods to solve the full potential equation, the Euler equations, and the Navier-Stokes equations, have become available.⁴⁻¹⁴ In general, the full potential and Euler methods, like the singularity methods, have the advantage that they are relatively efficient computationally and are quite useful in some applications where viscous effects are not domi-

nant. However, a disadvantage is that, for computing rotor-fuselage interactional effects that include viscous effects, a boundary layer coupling model must be employed with these methods. To fully integrate the viscous computation, Navier-Stokes methods should be employed. Only a few examples of Navier-Stokes computations are present in the literature. In one of these, Meakin¹⁴ used the Navier-Stokes equations to compute the time-accurate flowfield around a V-22 tiltrotor vehicle, including the rotor. This computation was primarily geared toward demonstrating moving, chimera grid technology and is not currently a practical capability due to the large CPU times required. In general, solutions to the Navier-Stokes equations for interactional aerodynamics problems, where everything is modeled in one large computation, are not currently practical for routine use.

Hybrid Methods

With the expense of Navier-Stokes methods for compete rotorcraft out of reach for routine computations, a practical, engineering solution is to use a hybrid approach. In hybrid approaches, several different methods complement each other. For example, Steinhoff, *et al.*¹⁵ combined a vorticity capturing method with a Navier-Stokes method to reduce artificial dissipation effects on rotor wake vortices, which in turn relaxes the grid resolution requirement to resolve and maintain a rotor wake vortex in the solution procedure. Boyd and Barnwell¹⁶ first introduced a hybrid method that loosely couples a Generalized Dynamic Wake Theory¹⁷⁻²⁰ (GDWT) with a Navier-Stokes method. Boyd³ extended that method to include both a fuselage and a rotor and computed unsteady fuselage surface pressures and unsteady inflow for a complete configuration.

The current work uses the method of Boyd³ and presents results using that method. Below, a brief description of the method is provided for completeness.

Computational Method

The current computation method is a hybrid method that loosely couples the GDWT to a Navier-Stokes method, OVERFLOW. The details of this coupling can be found in Boyd,³ but a brief outline is presented here.

As discussed earlier, determination of the gross loading and rotor trim requires many revolutions of the rotor. As such, this computationally expensive portion of the method is separated from the CFD portion of the computation. This separation greatly reduces the time spent on time-accurate computations in the CFD portion of method. Based on the above assumption, the current method splits the interactional aerodynamics problem into three distinct pieces: (1) the Rotor Loading

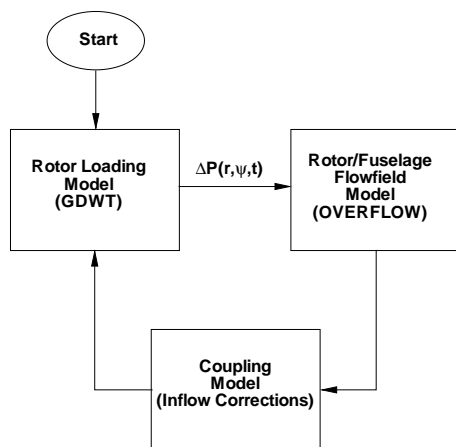


Figure 2. Current hybrid method.

Model, (2) the Rotor/Fuselage Flowfield Model, and (3) the Coupling Model. The arrangement of these pieces is shown in figure 2.

Rotor Loading Model

To reduce the computational expense of the entire process, a model is used to determine the loading distribution on and the trim state of the helicopter rotor. The model used here is based on the GDWT as discussed above. This model uses a solution of the Laplace equation for a isolated, circular wing developed by Kinner.²¹ Essentially, Kinner's solution provides admissible acceleration potential functions on the circular wing. To determine the unknown coefficients in Kinner's solution, Peters, Boyd, He,¹⁸ He,¹⁷ and Peters and He,¹⁹ used the linearized Euler equations, the continuity equation, and special rotor boundary conditions, to relate the Kinner acceleration potential to the induced inflow at the rotor disk. For the current research, the resulting closed form matrix equations are iteratively solved in conjunction with a modified Newton-Raphson trim technique to determine the unsteady induced inflow, the trim state, and the unsteady loading distribution of the isolated rotor.

With the solution of the GDWT for the isolated rotor, the "Rotor Loading Model" portion of figure 2 is complete. In figure 2 it can be seen that the pressure (loading) distribution from the Rotor Loading Model is used in the "Rotor/Fuselage Flowfield Model".

Rotor/Fuselage Flowfield Model

Now, with a known pressure distribution on the rotor disk, a Rotor/Fuselage Flowfield Model is used to solve the Navier-Stokes equations. For this model, a thin-layer, Navier-Stokes code (OVERFLOW²²) has been modified to include an unsteady boundary condition. For this new boundary condition, a cylindrical, non-rotating grid is

used to represent the rotor. The predetermined pressure distribution is applied as an additional term in the energy equation as follows:

$$\Delta(p_{e0}) = \frac{A(\bar{r})\Delta P}{\gamma - 1} \quad (1)$$

where equation (1) is in terms of the non-dimensional quantities used in OVERFLOW and $A(\bar{r})$ is the ratio between the local actual blade area and the local computational cell area at a given radial station on the blade. This ratio is used to maintain the correct overall thrust. The additional conservative energy term in equation (1) is then split into two parts. One half of the term is applied to the "upper rotor plane" (see figure 3b) and the negative of the other half of the term is applied to the "lower rotor plane". This procedure effectively creates a pressure jump between two planes in the rotor grid, separated by an "iblaned plane" which ensures that the artificial dissipation terms, which operate on a pressure discontinuity, do not modify the input pressure distribution at the rotor plane. All remaining flow quantities on the upper and lower rotor planes are determined by averaging the quantities at planes "A" and "B" in figure 3b. Figure 3a shows a top view of the rotor grid used in figure 3b. In this top view, a rectangular section is used to represent the actual blade area, and a shaded wedge represents the computational area (these areas are not to scale). Only one blade is represented in this figure.

For a multibladed rotor, one of these computational wedges exists for each blade. A radially varying, additional conservative energy term is applied along each of these computational wedges for each blade. At each time step in the time-accurate solution procedure, the pressure jump "travels" around the rotor azimuth direction, one grid line per time step. This unsteady boundary condition effectively represents the rotor blades as a pressure jump traveling around the rotor azimuth on a non-rotating, cylindrical grid.

Using the chimera grid techniques available in OVERFLOW, the above rotor grid is combined with other grids which represent the fuselage and the remaining flowfield. OVERFLOW then solves the time-accurate, thin-layer Navier-Stokes equations on this set of grids, along with the unsteady, pressure jump boundary condition. The solution procedure is executed until the initial transients are removed and a periodic flowfield is obtained.

Since the specified pressure jump was originally determined by an isolated rotor model, the pressure jump boundary condition does not represent the combined rotor-fuselage system. Therefore, once a periodic solution has been obtained with the original pressure jump boundary condition, an "Inflow Correction" method is used to account for the presence of the fuselage in the Rotor Loading Model. Discussion of this method is be-

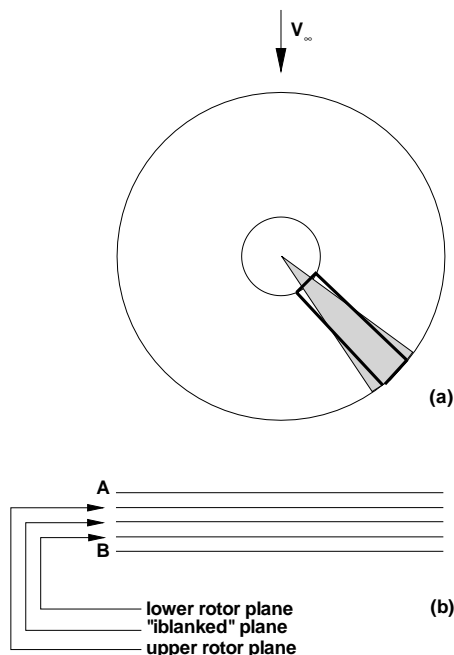


Figure 3. Schematic of new boundary condition.

yond the scope of this paper, but is discussed in detail in Boyd.³ Figure 2 shows the location of the “Coupling Model (Inflow Corrections)” portion of the model.

With these inflow corrections, the GDWT model is re-executed to obtain a new unsteady pressure jump boundary condition that has been corrected to account for the presence of the fuselage. This cycle is repeated until there is no significant solution change between iterations.

Results

Experimental Setup

Results from the computational method discussed above will be compared to experimental data. The experiments used here are discussed in other references,^{3,23} but are discussed briefly here for completeness. There are two experiments that are used here. The first experiment (“Experiment 1”), reported by Elliott, Althoff, and Sailey,²³ used a Laser Velocimetry (LV) system to measure the induced inflow in a plane that was one rotor blade chord above the rotor tip path plane. These measurements were carried out for the combination of a generic helicopter fuselage (known as the ROtor Body Interaction (ROBIN) fuselage) and a four-bladed, rectangular rotor system in the NASA Langley Research Center 14- by 22-Foot Subsonic Tunnel (see figure 4).



Figure 4. Laser velocimeter experiment, NASA Langley Research Center 14- by 22-Foot Subsonic Tunnel.

The LV measurements were processed at an azimuthal resolution of approximately 2.8° . Comparisons to both the time-averaged and the time dependent measured data will be made subsequently.

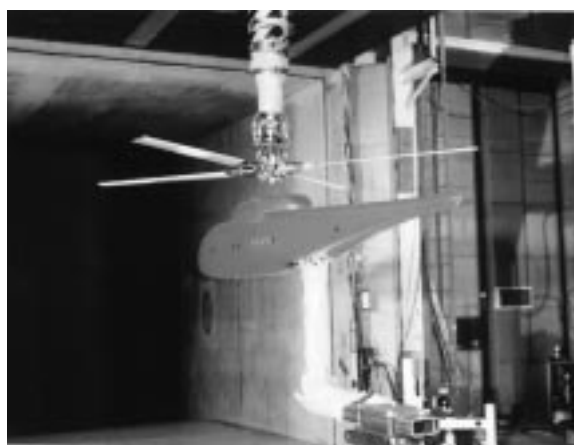


Figure 5. Unsteady surface pressure experiment, NASA Langley Research Center 14- by 22-Foot Subsonic Tunnel.

The second experiment (“Experiment 2”) used here was carried out by the third author and her colleagues, again using the ROBIN fuselage with the same rectangular rotor system. The primary difference in the configuration between the first and second experiments is that, in the first experiment, the rotor drive system was contained inside the fuselage shell, whereas, in the second experiment, the rotor and fuselage were mounted on separate systems. That is, in the second experiment, the rotor drive system was mounted to the tunnel ceiling and the fuselage was sting mounted on a post attached to the tunnel floor (see figure 5). This experiment was conducted in two phases: (1) an isolated rotor configuration (with the fuselage lowered to the tunnel floor) and (2) a rotor/fuselage configuration (with the fuselage in place). In the first phase of this test, unsteady inflow measurements were made at a limited number of locations on the advancing side of the rotor, one chord above the tip path

plane. In the second phase of the experiment, unsteady surface pressures were measured along the top centerline of the fuselage and at several locations on the sides of the fuselage. The data presented here are a small subset of the total data taken in the second experiment. Subsequent comparisons will be made to these unsteady inflow and unsteady surface pressure data. Table 1 lists several of the operating conditions and rotor parameters associated with both Experiments 1 and 2.

Table 1. Operating conditions and rotor parameters.

Property	Value
Blade planform	Rectangular
radius	0.8606 meters
root chord	0.0660 meters
tip chord	0.0660 meters
number of blades	4
root cutout location	0.24R
flap/lag hinge location	0.06R
airfoil section	NACA 0012
twist	-8°
nominal thrust coefficient	0.0065
solidity	0.0977
nominal hover M_{tip}	0.55
approx. mean coning angle	1°
shaft tilt	3° nose down

Induced Inflow Comparisons

Time-Averaged Induced Inflow

Once the iteration procedure has concluded, as discussed in Boyd,³ comparisons between a number of quantities are possible. For these comparisons, the current model was executed with and without a fuselage in the solution procedure. As shown in Boyd and Barnwell¹⁶ and Boyd,³ the current model is also applicable to an isolated rotor configuration (*i.e.*, no fuselage).

First, a comparison is presented between the measured and predicted, time-averaged induced inflow. Inflow ratio is defined as the local velocity divided by the rotor tip speed. The measurement data are from Experiment 1 at a plane that is one blade chord above the tip path plane of the rotor at a rotor advance ratio of $\mu = 0.23$. The predicted results are from the same location above the rotor tip path plane and are at the same operating condition used in Experiment 1. The rotor tip speed is used to make the data and predicted results nondimensional.

Figure 6a shows the measured, time-averaged induced inflow ratio parallel to the rotor tip path plane from Experiment 1. These experimental data show an induced inflow pattern that is not symmetric between the advancing and retreating sides of the rotor. For example, the contour

line with a value of 0.015 shows that the induced inflow is asymmetric about the fore-aft plane of the rotor. Figure 6b shows the predicted, time-averaged induced inflow ratio parallel to the rotor tip path plane for the isolated rotor configuration. Although the magnitudes are similar to the measured values, the inflow distribution does not match the measured distribution well. Here, unlike the measured data, the predicted induced inflow is somewhat symmetric between the advancing and retreating sides of the rotor. Figure 6c shows the predicted, time-averaged induced inflow ratio parallel to the rotor tip path plane for the full rotor-fuselage configuration. It is seen that the fuselage has a large impact on the inflow distribution. As with the isolated rotor configuration, the magnitude of the inflow matches the measured data well. In addition, the distribution of inflow now matches the experimental data well, including the asymmetric pattern seen in the measured data. Figure 6d shows the difference between the full rotor-fuselage configuration and the isolated rotor configuration. This difference plot shows the effect of the fuselage on the in-plane induced inflow. As would be expected for a fuselage, there is a deceleration of the flow over the forward portion of the rotor disk due to the upward slope of the nose of the fuselage and a subsequent re-direction of the flow. Over the rear portion of the rotor disk, there is an acceleration of the flow due to the downward slope of the rear portion of the pylon.

Figure 7a shows the measured, time-averaged induced inflow ratio perpendicular to the rotor tip path plane from Experiment 1. These measured data show several typical features of time-averaged induced inflow. First, there is an upwash on the forward portion of the rotor disk. Second, there is an increased downward inflow toward the rear portion of the disk with concentrations in the first and fourth rotor quadrants. Figure 7b shows the predicted, time-averaged induced inflow ratio perpendicular to the rotor tip path plane for the isolated rotor configuration. This configuration exhibits many of the same features as the measured data. For example, there is an upwash on the forward portion of the rotor disk, but that upwash is not as prominent as in the measured data. Figure 7c shows the predicted, time-averaged induced inflow ratio perpendicular to the rotor tip path plane for the full rotor-fuselage configuration. The magnitude as well as the inflow distribution is well matched when the fuselage is included in the computation. Figure 7d shows the difference between the full rotor-fuselage configuration and the isolated rotor configuration. Again, this figure displays features that are expected due to the presence of a fuselage. For example, there is an increased upwash over the forward portion of the disk as the flow is deflected upward over the nose of the fuselage, and there is an increased downwash at the rear of the rotor disk, just aft of the pylon, as the flow accelerates downward just

behind the fuselage pylon.

Time-Accurate Induced Inflow

The previous section showed that the time-averaged induced inflow in the parallel and perpendicular directions (relative to the rotor tip path plane) are well predicted by the current unsteady method. This section will present comparisons of the measured and predicted unsteady inflow data corresponding to the same flight conditions used in Experiment 1. The measured data presented here is from the first phase of Experiment 2 (isolated rotor configuration).

Figure 8 shows the measured and predicted unsteady induced inflow ratios. These inflow ratios are at an azimuthal location of $\psi = 84^\circ$ and a blade radial location of $r/R = 0.80$. Both the isolated rotor and combined rotor-fuselage configuration are shown. Both components are well predicted, especially the inplane component. For this particular location, the presence of the fuselage has only a minor impact on the predicted unsteady induced inflow. Previous literature has shown^{3,16} that these induced inflow ratios are typically well predicted over the entire rotor disk.

Unsteady Surface Pressure

In Experiment 2, unsteady surface pressure measurements were made for the same flight configuration and the same flight conditions as in Experiment 1. These measurements were made along the top centerline of the fuselage and at several locations on the sides of the fuselage. Comparisons are made here between the measured and predicted unsteady surface pressures along the top centerline and at several locations on the advancing and retreating sides of the fuselage. These pressure taps on the sides of the fuselage were located at several vertical locations and at a constant 44% of the fuselage length.

For these comparisons, a modified pressure coefficient is used. This modified pressure coefficient is defined in equation (2) and is used to avoid numerical problems associated with the definition of the standard pressure coefficient when the freestream velocity approaches zero (as would be the case in hover).

$$C'_p = \frac{100(P - P_\infty)}{\frac{1}{2}\rho(\Omega R)^2} \quad (2)$$

In equation (2), P is the local pressure, P_∞ is the freestream pressure, ρ is the freestream density, ΩR is the rotor tip speed, and the factor of 100 is included for numerical convenience. For reference, equation (3) shows the relation between the standard pressure coefficient and the modified pressure coefficient used here.

$$C'_p = 100\mu_\infty^2 C_p \quad (3)$$

In equation (3), μ_∞ is the standard rotor advance ratio and C_p is defined in the usual way.

Figure 9 shows a comparison of the unsteady component of the measured and predicted modified pressure coefficient on the top centerline of the fuselage at various stations along the length of the 2 meter long fuselage. The location of the reference blade is plotted along the horizontal axis, and the negative of the modified pressure coefficient is plotted along the vertical axis. Since this is a four-bladed rotor, a dominant pressure pulse can be seen at a frequency of four pulses per rotor revolution. This is indicative of the four blades individually passing over each measurement location. It can be seen that the phase of each of the predictions matches the measured phase well; however, the amplitudes are slightly over-predicted.

Figure 10 shows a comparison of the unsteady component of the measured and predicted modified pressure coefficient on the left and right sides (retreating and advancing sides, respectively) of the fuselage at a constant downstream location of $x = 0.8809$ meters ($x/L \approx 0.44$) for several vertical locations. Again, the reference blade location is on the horizontal axis, and the negative of the modified pressure coefficient is on the vertical axis. The retreating side comparisons show that the unsteady pressures are slightly overpredicted, while the advancing side unsteady pressures are well matched in magnitude and phase.

Conclusions

A novel computational model for unsteady rotorcraft interactional aerodynamics has been presented. This new hybrid model couples a rotor loading model and a rotor/fuselage flowfield model in a manner that is efficient and capable of predicting time-averaged and time-accurate rotor inflow ratios and unsteady surface pressures on the fuselage due to blade passages.

References

1. Sheridan P.F. and R.P. Smith. *Interactional Aerodynamics - A New Challenge to Helicopter Technology*. Washington, D.C., May 1979. *Presented at the 35th Annual American Helicopter Society Forum*.
2. W. Johnson. Recent Developments in Rotary-Wing Aerodynamic Theory. *AIAA Journal*, 24(8):1219–1244, August 1986.
3. D.D. Boyd, Jr. *Rotor-Fuselage Interaction Aerodynamics: A New Computation Model*. PhD thesis, Virginia Polytechnic Institute and State University, July, 1999.
4. C.S. Chen and J.O. Bridgeman. *Three-Dimensional Viscous Rotor Flow Calculations Using Boundary Layer Equations*. Amsterdam, Netherlands, September.

- ber 12-15, 1989. *Presented at the 15th European Rotorcraft Forum.*
5. J.O. Bridgeman, D.S. Prichard, and F.X. Caradonna. The Development of a CFD Potential Method for the Analysis of Tilt-Rotors. In *Proceedings of the AHS Technical Specialists Meeting on Rotorcraft Acoustics and Fluid Dynamics*, Philadelphia, PA, October 15-17, 1991.
 6. R.C. Strawn. Wing-Tip Vortex Calculations with an Unstructured Adaptive-Grid Euler Solver. In *Proceedings of the 47th Annual American Helicopter Society Forum*, Phoenix, AZ, May 1991.
 7. T.J. Barth. A 3-D Upwind Euler Solver for Unstructured Meshes. Honolulu, HI, June 1991. Paper AIAA-91-1548.
 8. R.C. Strawn and T.J. Barth. A Finite-Volume Euler Solver for Computing Rotary-Wing Aerodynamics on Unstructured Meshes. In *Proceedings of the 48th Annual American Helicopter Society Forum*, Washington, D.C., June 1992.
 9. L.A.J. Zori and R.G. Rajagopalan. Navier-Stokes Calculations of Rotor-Airframe Interaction in Forward Flight. Washington, D.C., June 1992. *Presented at the 48th Annual American Helicopter Society Forum.*
 10. R.G. Rajagopalan and Z. Zhaoxing. Performance and Flow Field of a Ducted Propellor. Monterey, CA, July 10-12, 1989. *Presented at the AIAA/ASME/SAE/ASEE 25th Joint Propulsion Conference.*
 11. R.G. Rajagopalan and S.J. Mathur. Three Dimensional Analysis of a Rotor in Forward Flight. *Journal of the American Helicopter Society*, July 1993.
 12. M.S. Chaffin and J.D. Berry. Navier-Stokes Simulation of a Rotor Using a Distributed Pressure Disk Method. In *Proceedings of the 51st Annual American Helicopter Society Forum*, volume I, pages 112–136, Ft. Worth, TX, May 1995.
 13. J.D. Berry, V.B. Letnikov, I. Bavykina, and M.S. Chaffin. A Comparison of Interactional Aerodynamics Methods for a Helicopter in Low Speed Forward Flight. In *Proceedings of the 23rd European Rotorcraft Forum*, volume I, pages 33.1–33.9, Dresden, Germany, September 16-18, 1997.
 14. R. Meakin. Moving Body Overset Grid Methods for Complete Aircraft Tiltrotor Simulations. Orlando, FL, June 6-9, 1993. *Presented at the 11th AIAA Computational Fluid Dynamics Conference.*
 15. J. Steinhoff, W. Yonghu, T. Mersch, and H. Senge. Computational Vorticity Capturing: Application to Helicopter Rotor Flow. In *30th Aerospace Sciences Meeting and Exhibit*, Reno, NV, January 6-9, 1992. Paper AIAA-92-0056.
 16. D.D. Boyd, Jr. and R.W. Barnwell. Rotor-Fuselage Interactional Aerodynamics: An Unsteady Rotor Model. In *Proceedings of the 54th Annual American Helicopter Society Forum*, volume I, pages 23–44, Washington, D.C., May 20-22, 1998.
 17. C.J. He. *Development and Application of a Generalized Dynamic Wake Theory For Lifting Rotors*. PhD thesis, Georgia Institute of Technology, Atlanta, GA, July 1989.
 18. D.A. Peters, D.D. Boyd, Jr., and C.J. He. Finite State Induced Inflow Model for Rotors in Hover and Forward Flight. St. Louis, MO, May 18-20, 1987. *Presented at the 43rd Annual American Helicopter Society Forum.*
 19. D.A. Peters and C.J. He. Correlation of Measured Induced Velocities with a Finite-State Wake Model. Boston, MA, May 1989. *Presented at the 45th Annual American Helicopter Society Forum.*
 20. D.A. Peters and C.J. He. Finite State Induced Inflow Models Part II: Three Dimensional Rotor Disk. *Journal of Aircraft*, Volume 32(Number 2), March-April 1995.
 21. W. Kinner. The Potential Theory of Airfoils of Circular Planform. *Ingenieur-Archiv*, 8(1):47–80, February 1937.
 22. P.G. Buning, D.C. Jespersen, T.H. Pulliam, W.M. Chan, J.P. Slotnick, S.E. Krist, and K.J. Renze. OVERFLOW User's Manual: Version 1.8, February 23 1998.
 23. J.W. Elliott, Susan L. Althoff, and R.H. Sailey. Inflow Measurement Made With a Laser Velocimeter on a Helicopter Model in Forward Flight - Volume II: Rectangular Planform Blades at an Advance Ratio of 0.23. NASA TM 100542, April 1988.

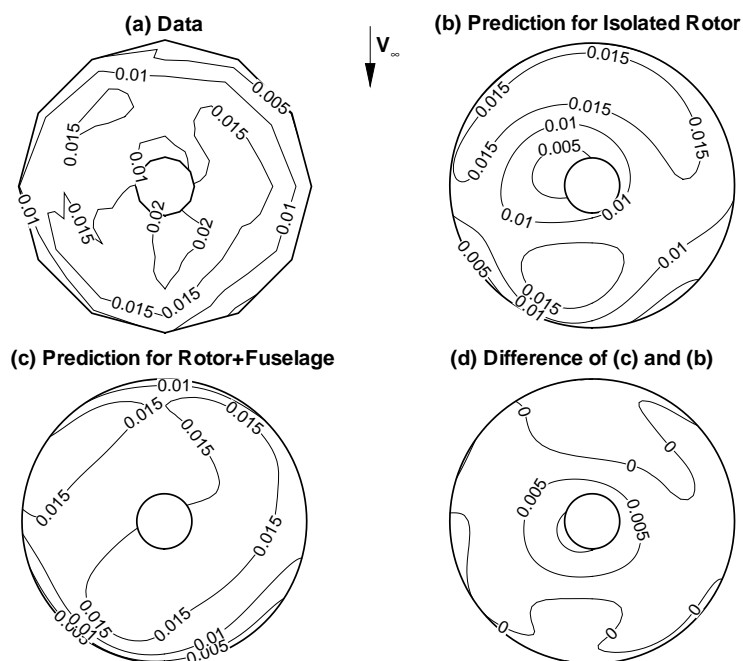


Figure 6. Measured and predicted time averaged parallel induced inflow ratio from time accurate computations.

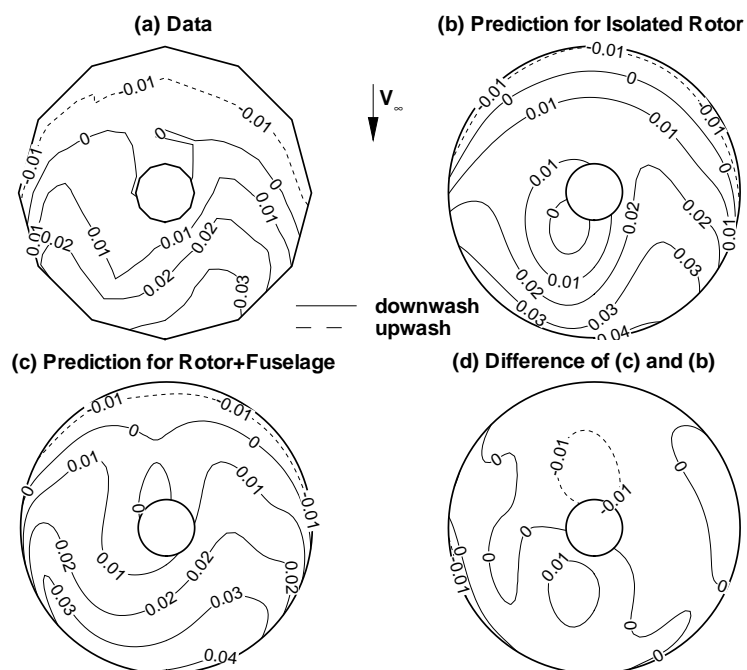


Figure 7. Measured and predicted time averaged perpendicular induced inflow ratio from time accurate computations.

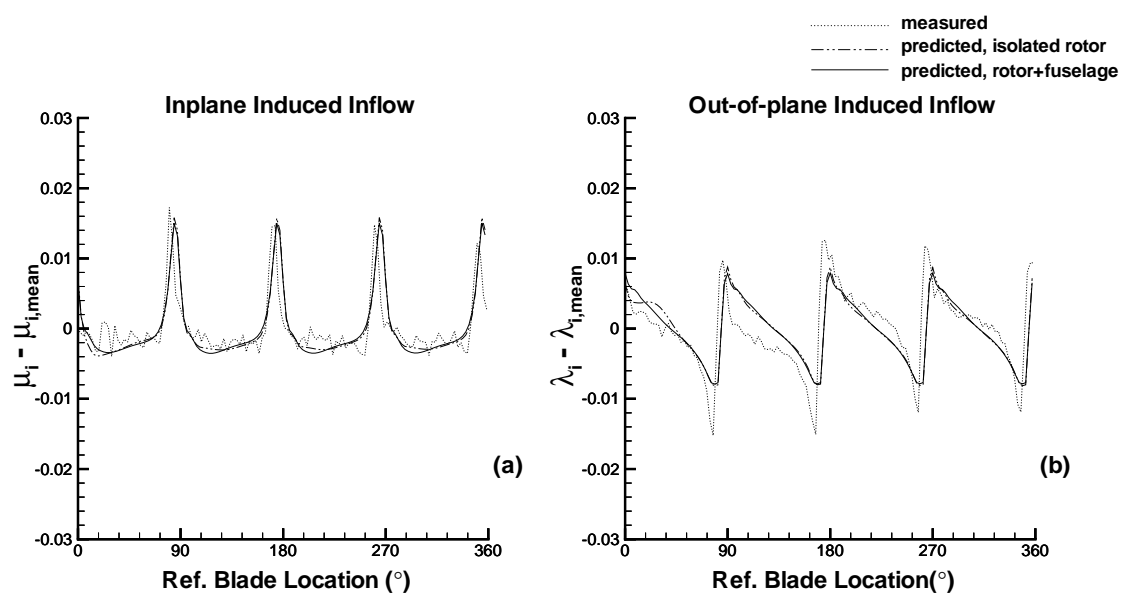


Figure 8. Measured and predicted induced inflow in two directions for an isolated rotor and a rotor/fuselage combination.

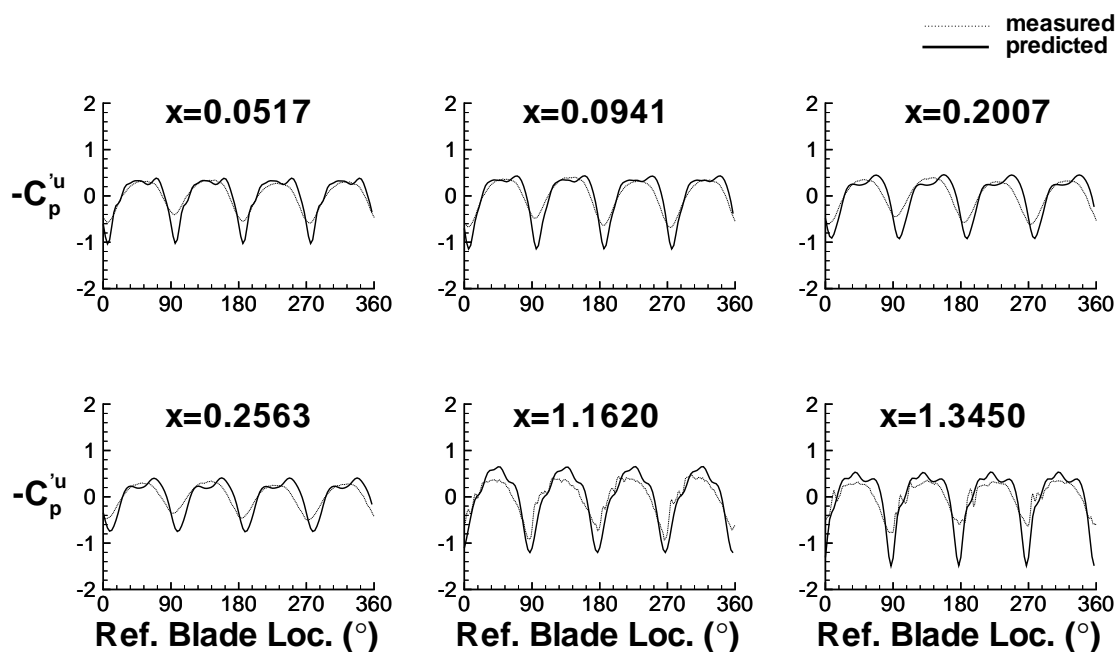


Figure 9. Measured and predicted unsteady modified pressure coefficient on the top centerline of the ROBIN fuselage. “x” denotes the distance in meters from the nose of the 2 meter long fuselage.

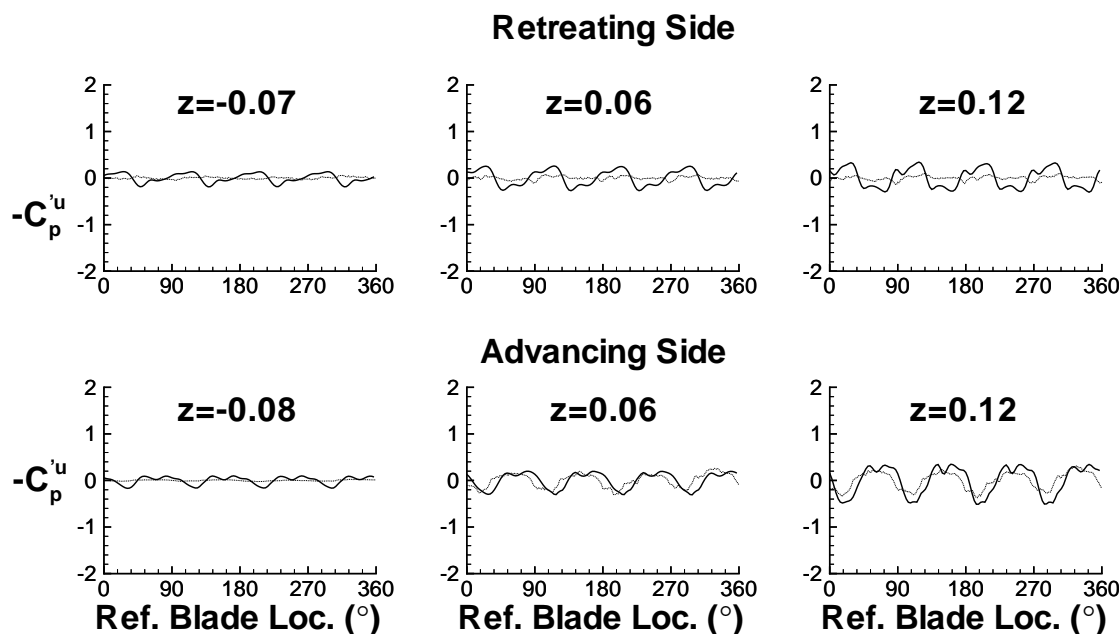


Figure 10. Measured and predicted unsteady modified pressure coefficient on the retreating and advancing sides of the ROBIN fuselage. “z” denotes the distance measured in meters from the horizontal reference line of the fuselage.